Available online at www.sciencedirect.com
SCIENCE DIRECT®
Journal of Solid State Chemistry 177 (2004) 3666–3674
JOURNAL OF SOLID STATE CHEMISTRY
http://elsevier.com/locate/jssc

Selective self-propagating combustion synthesis of hexagonal and orthorhombic nanocrystalline yttrium iron oxide

Ling Wu,[a] Jimmy C. Yu,[a,*] Lizhi Zhang,[a] Xinchen Wang,[a] and Siukong Li[b]

[a] *Department of Chemistry, The Chinese University of Hong Kong, Shatin, New Territories, Hong Kong, China*
[b] *Department of Physics, The Chinese University of Hong Kong, Shatin, New Territories, Hong Kong, China*

Received 6 May 2004; received in revised form 5 June 2004; accepted 9 June 2004

Available online 23 August 2004

Abstract

Macroporous nanocrystalline $YFeO_3$ was prepared by a self-propagating combustion method using yttrium nitrate and iron nitrate as precursors and glycine as a fuel. The phase structure of the product can be selectively controlled to be hexagonal or orthorhombic by simply adjusting the ratio of glycine to nitrate. The samples were characterized by X-ray diffraction (XRD) analysis, N_2 adsorption, micro-Raman spectroscopy, Fourier transform infrared absorption spectroscopy (FT-IR), thermal analysis (TGA/DSC), scanning electron microscopy (SEM), high-resolution transmission electron microscopy (HRTEM), X-ray photoelectron spectroscopy (XPS), and magnetic property analysis. Photocatalytic activity for the degradation of methylene blue in water under visible light irradiation shows that the orthorhombic $YFeO_3$ is superior to the hexagonal form. More adsorbed oxygen and ferromagnetism of the orthorhombic sample may explain its high activity.

Keywords: Self-propagating combustion; Nanocrystalline yttrium iron oxide; Hexagonal structure; Orthorhombic structure; Photocatalysis

1. Introduction

Synthesis of nanosized materials is one of the major challenges in the development of advanced functional materials because they exhibit unique properties conferred by particles of very small dimensions in contrast to the corresponding bulk materials [1,2]. The high specific surface area and the increased volume fraction of atoms located on the surface and at the grain boundaries result in an increased surface energy. Therefore, surfaces and interfaces of nanosized materials provide an active substrate for physical, chemical, and biological reactions, including industrial catalysis [3,4]. Moreover, optical, electronic and magnetic properties can be tailored to specific applications, leading to a burgeoning nanotechnology industry [5,6]. Rare earth orthoferrites ($LnFeO_3$) with perovskite-type structure, such as $YFeO_3$, exhibit interesting physical and chemical properties because of their ionic and electronic defects [7,8]. These materials are widely used in the fields of fuel cells [9], catalysts [10–12], gas sensors [13,14], magnetic materials [15,16], and environmental monitoring application [17].

Rare-earth orthoferrites are often prepared from high temperature solid-state reactions of the corresponding pure oxides [18]. However, this process suffers from problems such as excessive crystal growth, irregular atomic stoichiometric ratio, and formation of undesirable phases. Other synthesis routes have also been proposed including the precipitation method [19,20], thermal decomposition process [21], solvothermal treatment [22], sonochemical approach [23] and combustion route [24,25]. Self-propagating combustion synthesis is a fast, simple, and inexpensive process, which consists of an exothermic redox reaction between metal nitrates (act as oxidizing agents) and an appropriate fuel (a reducing agent). The main advantages are that the necessary heat for synthesis is obtained from the reaction itself and nanosized powders can be crystallized directly without

*Corresponding author. Fax: +852-2603-5057.
E-mail address: jimyu@cuhk.edu.hk (J.C. Yu).

0022-4596/$ - see front matter © 2004 Elsevier Inc. All rights reserved.
doi:10.1016/j.jssc.2004.06.020

the need for calcination post-treatment [26]. Therefore, this synthetic approach is an attractive method for commercial synthesis of complex inorganic oxides.

In this paper, nanocrystalline $YFeO_3$ with macroporous structure is prepared from an aqueous solution of yttrium nitrate, iron nitrate and glycine via a self-propagating combustion method. By adjusting the ratio of glycine to nitrates, hexagonal and orthorhombic nanocrystalline $YFeO_3$ can be selectively obtained. The structure, morphology, surface state and magnetic property of the hexagonal and orthorhombic nanocrystalline $YFeO_3$ were characterized and compared. The photocatalytic activity of the nanocrystalline $YFeO_3$ was also evaluated by the degradation of methylene blue in an aqueous solution under visible light irradiation.

2. Experimental

2.1. Synthesis

Analytical grade metal nitrates ($Y(NO_3)_3 \cdot 6H_2O$, $Fe(NO_3)_3 \cdot 9H_2O$) and glycine were dissolved in distilled water to form the precursor solution. The ratio of yttrium nitrate: iron nitrate: glycine: water was 1:1:1–1.7:30. The precursor solution was concentrated in a porcelain crucible on a hot plate at about 250°C under magnetic stirring. Water was gradually vaporized during heating. The foam produced was then ignited, giving a light brown voluminous and fluffy product in the container.

2.2. Characterization

X-ray diffraction (XRD) patterns were recorded by a Bruker D8 Advance X-ray diffractometer with Cu$K\alpha$ radiation at a scan rate of 0.02° $2\theta\,s^{-1}$. It was used to identify of the phase present and their crystallite size. The accelerating voltage and the applied current were 40 kV and 40 mA, respectively. The crystallite size was calculated from X-ray line broadening analysis by the Scherer equation: $D = 0.89\lambda/\beta\cos\theta$, where D is the crystal size in nm, λ is the Cu$K\alpha$ wavelength (0.15406 nm), β is the half-width of the peak in rad, and θ is the corresponding diffraction angle. The Brunauer–Emmett–Teller (BET) surface area (S_{BET}) were determined by nitrogen adsorption–desorption isotherm measurements at 77 K on a Micromeritics ASAP 2010 nitrogen adsorption apparatus. All the samples measured were degassed at 180°C before the actual measurements. Raman spectra of the powder samples on a glass slide were measured using a Renishaw 1000 micro-Raman system. A 50 times magnification objectives were selected. The excitation source used was an Argon ion laser operating at 514.5 nm with an output power of 20 mW. Infrared (IR) spectra on pellets of the samples mixed with KBr were recorded on a Nicolet Magna 560 FTIR spectrometer at a resolution of $4\,cm^{-1}$. Thermogravimetric analysis (TGA) and differential scanning calorimetry (DSC) were performed using a Netzsch STA 449C thermal analyzer, under air flow of 40 mL/min with a heating rate of 5°C/min from room temperature to 1000°C. The morphology of the samples was examined by using a scanning electron microscopy (SEM, LEO 1450VP). Phase identification and crystallite size measurements were also conducted using a high resolution transmission electron microscopy (JEOL2010F) with 200 kV accelerating voltage. The powder particles were supported on a carbon film coated on a 3 mm diameter fine-mesh copper grid. A suspension in ethanol was sonicated, and a drop was dropped on the support film. X-ray photoelectron spectroscopy (XPS) measurements were performed on a PHI Quantum 2000 XPS System with a monochromatic Al$K\alpha$ source and a charge neutralizer; all the binding energies were referenced to the C 1s peak at 284.8 eV of the surface adventitious carbon. The magnetic properties were measured using a vibrating sample magnetometer (VSM Lakeshore Model 7300) in room temperature.

2.3. Photocatalytic activity

Visible-light photocatalytic activities of the samples were measured by the decomposition rate of methylene blue in an aqueous solution. A 300 W tungsten halogen lamp was positioned inside a cylindrical Pyrex vessel and surrounded by a circulating water jacket (Pyrex) to cool the lamp. A cutoff filter was placed outside the Pyrex jacket to completely remove all wavelengths shorter than 400 nm to ensure irradiation with visible light only. Moreover, a saturated cupric acetate solution as a filter was placed in front of a reactor to absorb wavelengths longer than 580 nm. 0.1 g of photocatalyst was suspended in a 100 mL aqueous solution of 0.1 mM methylene blue. Prior to irradiation, the suspensions were magnetically stirred in the dark for ca. 1 h to reach adsorption/desorption equilibrium, and then 1 mL of a 30% hydrogen peroxide solution was added. At specific irradiation time intervals, 4 mL of the suspensions were collected, then centrifuged, and filtered through a Millipore filter (pore size, 0.22 in) to separate the photocatalyst particles. The solutions were analyzed by a Varian Cary 100 Scan UV-Visible spectrophotometer and the absorption peak at 663 nm was monitored.

3. Results and discussion

3.1. Synthesis

In this self-propagating combustion process, glycine acts as the fuel and it is oxidized by the nitrate ions.

Stoichiometrically balanced, the exothermic reaction can be expressed as follows:

$$3Y(NO_3)_3 + 3Fe(NO_3)_3 + 10NH_2CH_2COOH + 18O_2 \rightarrow 3YFeO_3 + 5N_2 + 18NO_2 + 20CO_2 + 25H_2O$$

It is well known that reaction temperature has a strong effect on the phase structure and particle sizes of the products. Lower temperatures may lead to metastable phase products with smaller particle size. By adjusting the ratio of glycine to nitrates (G/N), the combustion flame temperature can be controlled. It has been reported that the temperature for 1.7, 1.3 and 1.0 G/N ratio is about 1450°C, 1320°C and 1000°C, respectively [27]. In such a high temperature, the nanocrystalline $YFeO_3$ can be readily prepared. In our experiments, the glycine to nitrate ratio in the precursor solution varied from oxidant-rich (G/N: 0.85, 1.0, 1.3, 1.5 for samples S1, S2, S3, and S4, respectively) to stoichiometric (G/N: 1.7 for sample S5). Table 1 summarizes the results of nanocrystalline $YFeO_3$ obtained at different G/N ratios.

3.2. XRD and BET

Fig. 1a shows the XRD patterns of the as prepared products obtained by the present self-propagating combustion at different G/N ratios. The single broad peak with low intensity is only observed for sample S1 at G/N ratio of 0.85. This indicates that sample S1 mainly exists in an amorphous form. The pattern of sample S2 at G/N ratio of 1 shows four broad peaks at 2θ values of 30.3, 31.1, 51.9 and 61.5, which correspond to (101), (102), (110) and (114) crystal planes of hexagonal $YFeO_3$ (JCPDS 48-529). Moreover, the pattern of sample S3 at G/N ratio of 1.3 exhibits eight relative narrow peaks, which can be completely indexed to hexagonal structure of $YFeO_3$ (JCPDS 48-529). When the G/N ratio was increased to 1.5 for sample S4, the diffraction peaks match that of orthorhombic $YFeO_3$ (JCPDS 39-1489). The orthorhombic structure character of $YFeO_3$ was also observed from the XRD pattern of sample S5 at G/N ratio of 1.7, but the peak at 2θ value of 29.3 may attribute to body-centered cubic Y_2O_3. These results indicate that hexagonal and orthorhombic $YFeO_3$ can be selectively prepared by a adjusting the ratio of glycine to nitrates in a self-propagating combustion process. Hexagonal $YFeO_3$ can be formed in the range of 1–1.3 G/N ratios, while orthorhombic $YFeO_3$ is the main product at G/N ratios of 1.5 or higher. The orthorhombic structure (perovskite phase) is thermodynamically stable for all lanthanide elements. The hexagonal structure may exist in metastable phase for some lanthanides depending on their ionic radii [28]. For instance, hexagonal $YFeO_3$ can be prepared by calcination of a precursor gel obtained from the hydrolysis of an yttrium–iron double alkoxide [29] or from the glycothermal reaction of rare earth acetate and iron acetylacetonate [22]. In our preparation process, low values of G/N ratio favor the formation of hexagonal phase. This is probably due to the decrease in flame temperature at low G/N ratios. By comparing with other preparation methods, self-propagating combustion process is a simple, rapid and economic method to prepare $YFeO_3$. The average crystallite sizes calculated from the Scherer equation are 6.3, 20, 50, and 50 nm for samples S2, S3, S4, and S5, respectively (Table 1). The crystal size increases with the value of the G/N ratio. This is expected, because a high G/N ratio would result in an elevated combustion temperature, favoring the growth of crystals. It is noted here that the crystal grain size of $YFeO_3$ prepared by self-propagating combustion is smaller than those of reported in literatures [2,22]. The phase structure and the average crystallite sizes of nanocrystalline $YFeO_3$ obtained at different G/N ratios are also summarized in Table 1.

Fig. 1b shows the XRD patterns of as-prepared and calcined S1, S3 samples. It is found that the thermal treatment of as-prepared S1 at 500°C for 2 h cannot change the amorphous nature of S1. After calcination at 800°C for 2 h, the as-prepared S1 changes from amorphous to orthorhombic $YFeO_3$. However, the hexagonal structure of the as-prepared S3 does not change after the same treatment. This indicates that the hexagonal structure of $YFeO_3$ is rather stable, and the amorphous powders obtained from self-propagating combustion method can be converted directly to orthorhombic $YFeO_3$ at 800°C without going through the formation of hexagonal phase.

The BET specific surface areas of the as-prepared $YFeO_3$ samples are listed in Table 1. The hexagonal

Table 1
Phase structure, crystallite size and surface area of $YFeO_3$ samples at different G/N ratios

Samples	G/N (mole ratio)	Phase structure	Crystalline size (nm)	S_{BET} (m^2g^{-1})
S1	0.85	Amorphous	—	—
S2	1.0	Hexagonal	6.3	39
S3	1.3	Hexagonal	20	18
S4	1.5	Orthorhombic	50	6.4
S5	1.7	Orthorhombic	50	4.3
S1-500	0.85	Amorphous	—	—
S1-800	0.85	Orthorhombic	35	16

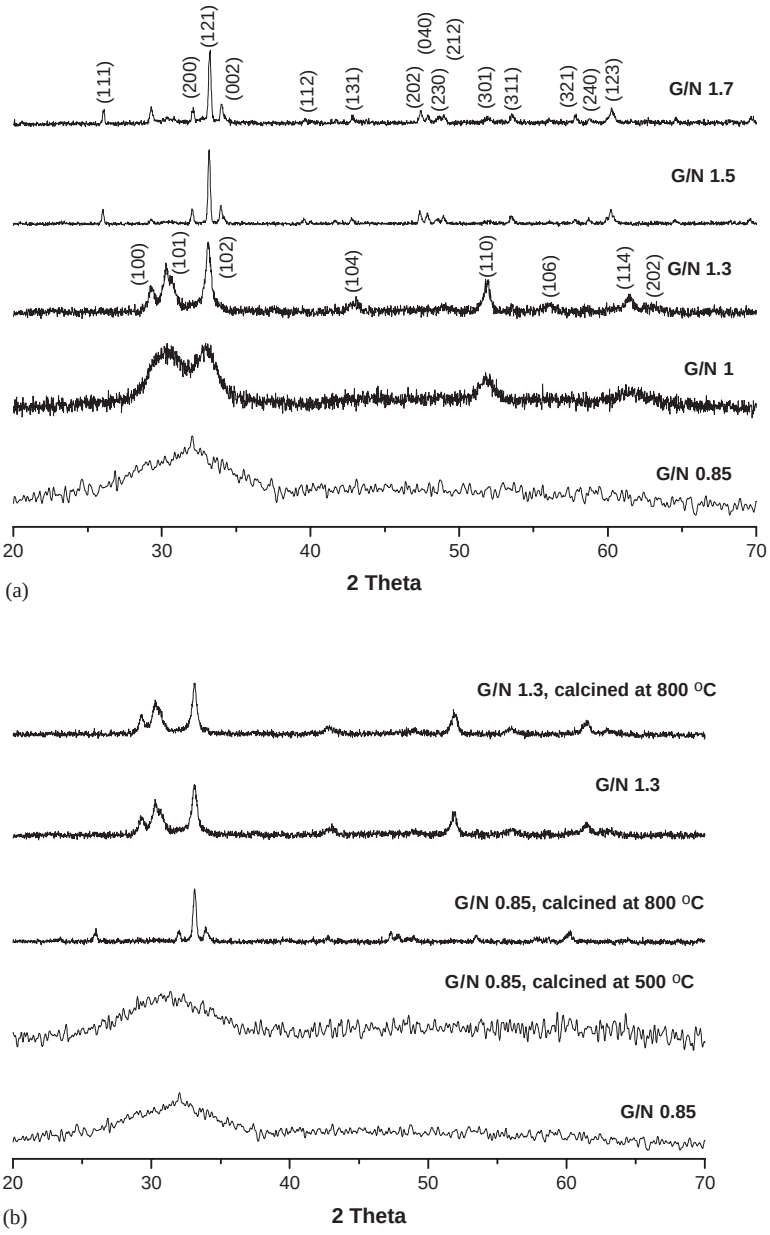

Fig. 1. (a) XRD patterns of the nanocrystalline $YFeO_3$ prepared by the self-propagating combustion method at G/N ratios of 0.85, 1, 1.3, 1.5, and 1.7. (b) XRD patterns of as-prepared samples S1 and S3 and their powders calcined at selected temperatures for 2 h.

phase $YFeO_3$ is smaller in crystallite size and therefore possesses a much higher surface area than the orthorhombic. Two representative samples, the hexagonal S3 and orthorhombic S4, were chosen for further characterization.

3.3. Spectroscopy and thermal analysis

Raman spectroscopy is a powerful method for phase structural analysis. It is more surface-sensitive than X-ray diffraction because its excitation energy is less penetrating than X-ray. Orthorhombic and hexagonal structures belong to different space groups, so they can be distinguished by Raman spectroscopy. Fig. 2 shows Raman spectra of the nanocrystalline $YFeO_3$ prepared by the self-propagating combustion method. The peaks for sample S3 with hexagonal phase are different from those of the sample S4 with orthorhombic phase. The spectrum of orthorhombic $YFeO_3$ is similar to that of orthorhombic $ReFeO_3$ [7,30–32]. Since the A_{1g} modes have frequencies very similar to that of the B_{1g} mode (within 1–2 cm^{-1}), we are not able to determine the contribution of each mode for orthorhombic $YFeO_3$. To our best knowledge, there is no report of the Raman

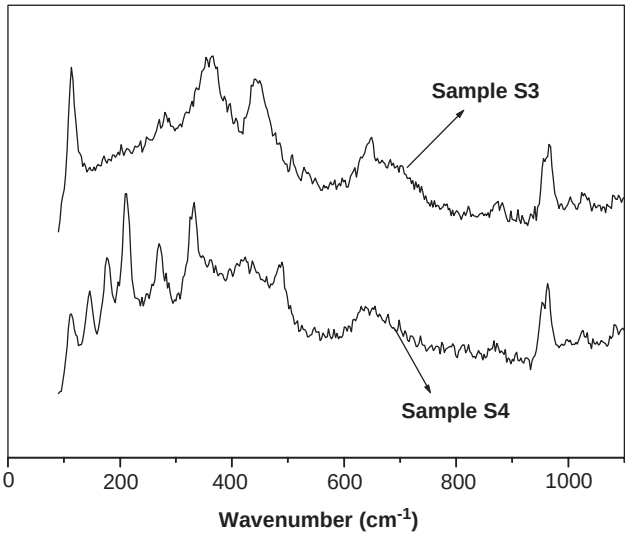

Fig. 2. Micro-Raman spectra of the nanocrystalline $YFeO_3$.

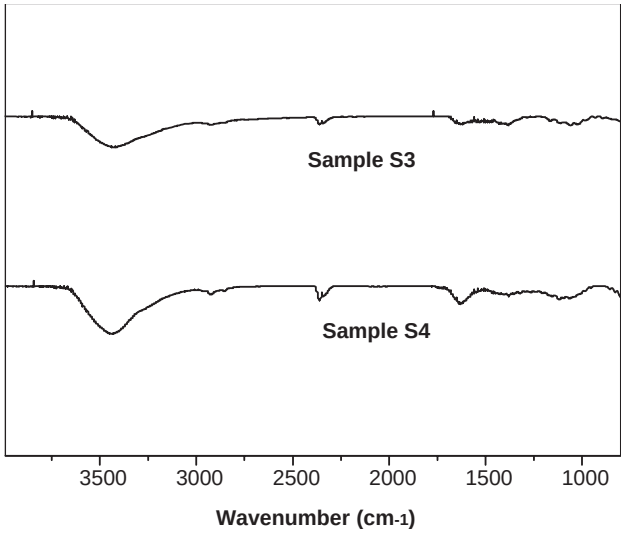

Fig. 3. FT-IR spectra of the nanocrystalline $YFeO_3$.

spectrum for hexagonal $YFeO_3$. A detailed study of the Raman spectrum for hexagonal $YFeO_3$ is worthwhile, but it is beyond the scope of this paper.

To examine whether the combustion is complete and to detect the presence of surface species in the as-prepared samples, FTIR spectra were recorded in the range of 900–4000 cm^{-1}. Fig. 3 shows that two absorption peaks are present in both spectra of samples S3 and S4, one at 3420 cm^{-1} and the other around 1630 cm^{-1}. These correspond to the surface-adsorbed water and oxygen species [33]. It should be noted that the two peaks in sample S4 is more intense than that of S3. Small characteristic CO_2 peaks at 2360 and 2337 cm^{-1} are also observed. Obviously, the sample S4 with orthorhombic phase can adsorb more water or oxygen species than that of the sample S3. There is no trace of residual organic species and nitrate anion.

The DTA and DSC curves of the as-prepared nanocrystalline $YFeO_3$ up to 1000°C are shown in Fig. 4. The TGA curves show weight losses of 5.6% and 3.8% below 500°C for sample S3 and S4, respectively, which may correspond to the adsorbed moisture in the samples. Then, the weight of the samples remains constant until the temperature reaches 1000°C. In the DSC curves, the most important aspect evident from the thermal studies is the absence of enthalpy changes at high temperatures for both samples S3 and S4, which implies that the combustion is complete and no organic species is present in the samples. There is no evidence of a phase transition taking place in the samples up to a temperature of 1000°C. The TGA-DSC data together with the FT-IR and XRD analytic results clearly demonstrate the effectiveness of the self-propagating combustion process in the preparation of pure phase nanocrystalline particles.

3.4. SEM and TEM

The typical SEM micrographs of the hexagonal and orthorhombic nanocrystalline $YFeO_3$ prepared by self-propagating combustion are shown in Fig. 5. SEM images reveal that both hexagonal and orthorhombic $YFeO_3$ are sponge-like and porous agglomerates with pore size of about 1–10 μm. The pores are formed by fast expulsion of gas during the combustion process.

The TEM images of the hexagonal and orthorhombic nanocrystalline $YFeO_3$ are shown in Fig. 6. The TEM image of sample S3 (Fig. 6a) reveals that the particles of hexagonal $YFeO_3$ are agglomerate with their average sizes at about 20 nm, in agreement with the XRD results. The HRTEM image (Fig. 6b) shows clear

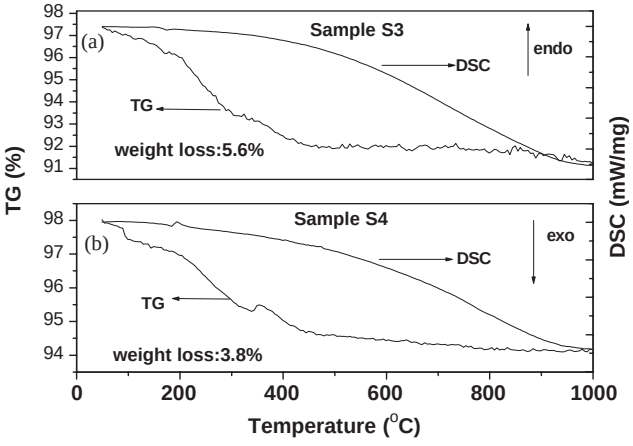

Fig. 4. DTA-DSC curves of the nanocrystalline: (a) sample S3 and (b) sample S4.

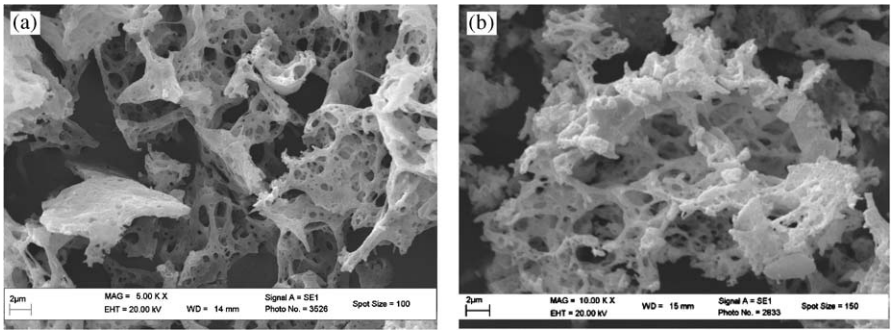

Fig. 5. SEM micrographs of the nanocrystalline $YFeO_3$: (a) sample S3 and (b) sample S4.

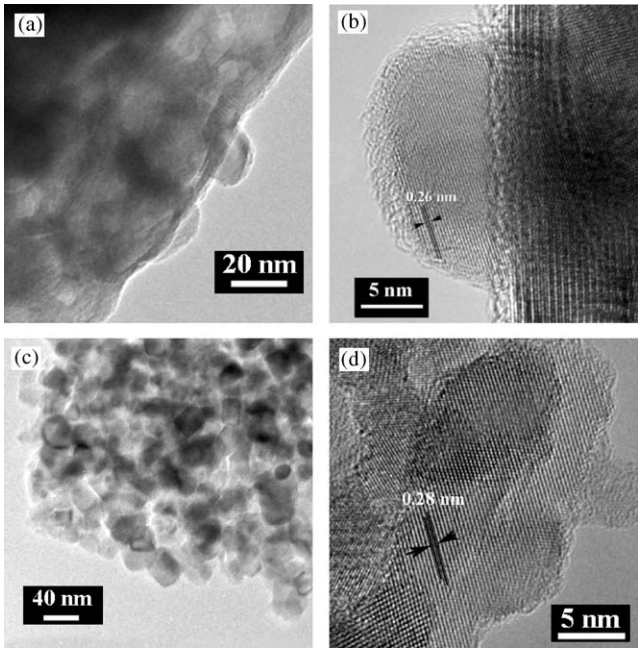

Fig. 6. TEM and HRTEM images of the nanocrystalline $YFeO_3$: (a, b) sample S3 and (c, d) sample S4.

lattice fringes, which allows for the identification of crystallographic spacing. The fringes of $d = 0.26$ nm match that of the (102) crystallographic plane of hexagonal $YFeO_3$. The TEM image of sample S4 (Fig. 6c) shows that the as-prepared particles are also agglomerate. The average particle size is estimated to be about 50 nm. This is in agreement with the results of XRD, and is much larger than that of sample S3 with hexagonal structure. The highly crystalline nanoparticles with clear lattice fringes are also observed in the HRTEM image (Fig. 6d). The fringes of $d = 0.28$ nm correspond the (200) or (121) crystallographic plane of the orthorhombic $YFeO_3$. Moreover, compositional analysis by transmission electron microscopy-energy dispersive X-ray spectroscopy (TEM-EDX) shows that both as-prepared samples have a homogenous distribution of the metals at the selected areas.

3.5. XPS

X-ray photoelectron spectroscopy (XPS) surface measurements were performed on nanocrystalline $YFeO_3$ powders to determine the elemental composition and oxidation state. Fig. 7 shows the Y 3*d*, Fe 2*p* and O 1*s* XPS peaks for the as prepared samples S3 and S4. Characteristic binding energy (BE) values of 156.6 eV for Y $3d_{5/2}$ and 158.6 eV for Y $3d_{3/2}$ (Fig. 7a) reveal a trivalent oxidation state for yttrium [34]. The Fe $2p_{3/2}$ and Fe $2p_{1/2}$ peaks in Fig. 7b are found at 710.9 and 724.4 eV, matching well with that of Fe^{3+} in Fe_2O_3 [2,34]. Moreover, The Fe 2*p* spectrum of Fe_2O_3 shows a satellite peak at 718.8 eV, which is a diagnostic feature for the Fe^{3+} species and is also present in the $YFeO_3$ samples. Fig. 7c shows the O 1*s* XPS peaks of samples S3 and S4. The peaks can be deconvoluted into two components, which are oxygen in lattice (O^{2-}) at a lower binding energy and surface adsorbed oxygen (O^{-}) at a higher bonding energy [35]. Obviously, there is more surface adsorbed oxygen (O^{-}) than lattice oxygen (O^{2-}) in both samples. It is also found that there is more surface adsorbed oxygen on the orthorhombic sample S4 than that on the hexagonal sample S3.

3.6. Magnetic property

Fig. 8 shows the magnetic hysteresis loops of the nanocrystalline $YFeO_3$ samples. The hysteresis plot for the hexagonal sample S3 shows a linear increase with field, with no sign of saturation up to 6000 Oe, resembling a paramagnet. The orthorhombic sample S4, however, almost reaches saturation at a magnetic field of 6000 Oe. This indicates that the orthorhombic sample is a weak ferromagnet, as in the case of orthoferrite [2,36,37]. These results confirm that $YFeO_3$

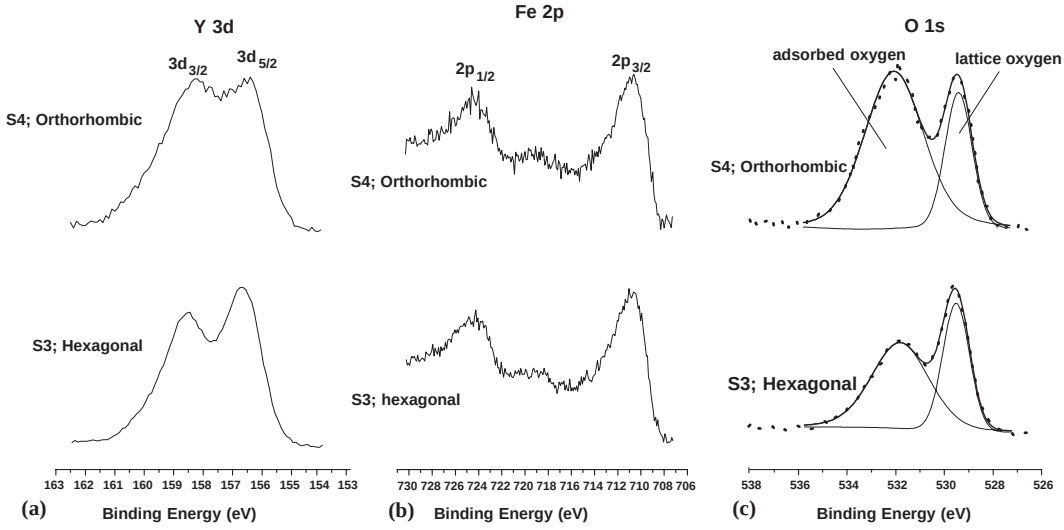

Fig. 7. High resolution XPS spectra of the nanocrystalline $YFeO_3$: (a) Y 3*d*, (b) Fe 2*p* and (c) O 1*s* (dotted lines are experiment results and solid lines are from curve fitting).

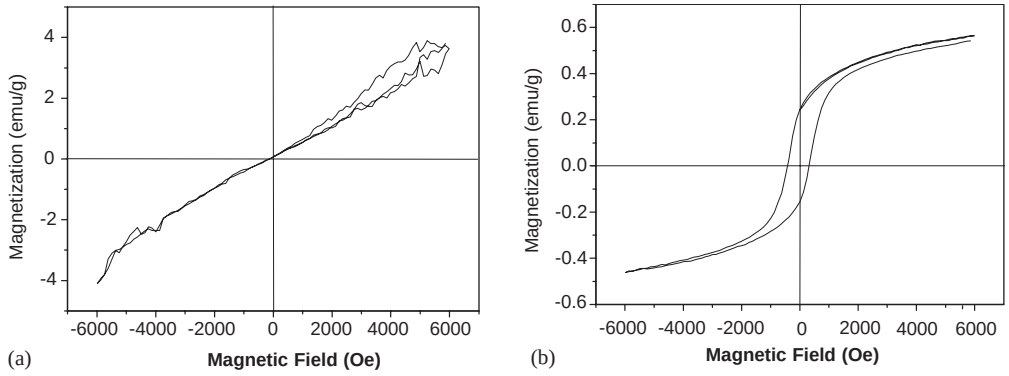

Fig. 8. The magnetization vs. applied field patterns: (a) sample S3 and (b) sample S4.

of different structures exhibits different magnetic properties.

3.7. Photocatalytic activity

$YFeO_3$ is a semiconductor material with a band gap of 2.6 eV [11]. It may be used as a photocatalyst that can be activated by visible light. We measured the photocatalytic activies of the hexagonal and orthorhombic $YFeO_3$ catalysts by the degradation of methylene blue (MB). It is shown in Fig. 9 that the degradation rate of MB under visible light irradiation is obviously enhanced for both hexagonal and orthorhombic nanocrystalline $YFeO_3$. This enhancement can be explained as follows. When visible light is illuminated on nanocrystalline $YFeO_3$, electrons are excited from the valence band to the conduction band. Then, the photogenerated electrons are migrated to the surface of $YFeO_3$ on which they can be scavenged by hydrogen peroxide to form hydroxyl radicals. The photogenerated holes can also react with adsorbed water to form hydroxyl radicals. The presence of ionic point defects such as oxygen vacancies in the $YFeO_3$ lattice would also affect its catalytic activity. Detailed discussion on the effects of solid-state defects has been reported and they are beyond the scope of this manuscript [38,39]. Curves *b* and *d* show that the activity of the orthorhombic sample (S4) is much higher than that of the hexagonal sample (S3). This can be explained by the availability of more adsorbed oxygen on the surface of orthorhombic $YFeO_3$, thus generating more hydroxyl radicals. Moreover, the ferromagnetism property of the orthorhombic $YFeO_3$ may help promote the separation of photogenerated electrons and holes. It has been reported that photocatalytic activity can be enhanced by the magnetic field effect [40]. In the control experiment, MB is only slightly degraded in the presence of hydrogen peroxide under visible light irradiation (curve *f*). The slight degradation of MB by $YFeO_3/H_2O_2$ in the dark (curves *a* and *c*) may due to the formation of hydroxyl radicals from the decomposition of H_2O_2 on $YFeO_3$. It is reported that some transition metal oxides, such as

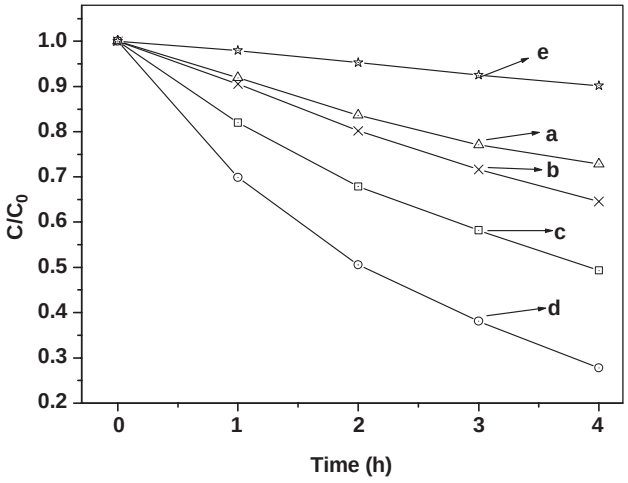

Fig. 9. Concentration changes of methylene blue measured at the maximum absorption wavelength of 663 nm during the degradation process in a $YFeO_3/H_2O_2$ suspension: (a) in the dark reaction for sample S3; (b) under visible light irradiation on S3; (c) in the dark reaction for sample S4; (d) under visible light irradiation on S4; and (e) under visible light irradiation but without $YFeO_3$.

FeOOH [41], TiO_2 [42], TS-1 and Ti-ZSM-5 [43], can react with hydrogen peroxide to produce hydroxyl radicals.

4. Conclusions

The experiments described here demonstrate the feasibility of direct preparation of highly nanocrystalline $YFeO_3$ particles with macropores by using a self-propagating combustion method without successive calcination. The hexagonal and orthorhombic $YFeO_3$ nanoparticles can be easily obtained by controlling the G/N ratio. The characterization results show that the samples have large surface areas, small nanoparticle sizes and abundant adsorbed oxygen. The magnetic property measurements indicate that the orthorhombic nanocrystalline $YFeO_3$ is ferromagnetic while the hexagonal nanocrystalline $YFeO_3$ is paramagnetic. Photocatalytic degradation of MB in water under visible light irradiation shows that the orthorhombic $YFeO_3$ is a superior photocatalyst.

Acknowledgments

The work was supported by the Research Grants Council (CUHK 4027/02P) of the Hong Kong Special Administrative Region. The authors express their thanks to Mr. Tzekin Cheung of the Hong Kong University of Science and Technology for HRTEM measurements.

References

[1] C.R. Martin, Science 266 (1994) 1961.
[2] S. Mathur, H. Shen, N. Lecerf, A. Kjekshus, H. Fjellvag, G.F. Goya, Adv. Mater. 14 (2002) 1405.
[3] A.T. Bell, Science 299 (2003) 1698.
[4] C. Suryanarayana, Bull. Mater. Sci. 17 (1994) 307.
[5] F.X. Redl, K.S. Cho, C.B. Murray, S. O'Brien, Nature 423 (2003) 968.
[6] M.C. Roco, J. Nanopart. Res. 3 (2001) 353.
[7] E. Traversa, P. Nunziante, L. Sangaletti, B. Allieri, L.E. Depero, H. Aono, Y. Sadaoka, J. Am. Ceram. Soc. 83 (2000) 1087.
[8] M. Cherry, M.S. Islam, C.R.A. Catlow, J. Solid State Chem. 118 (1995) 125.
[9] N.Q. Minh, J. Am. Ceram. Soc. 76 (1993) 563.
[10] M. Sharon, B.M. Prasad, Electrochim. Acta 19 (1985) 331.
[11] M.A. Butler, D.S. Ginley, M. Eibschutz, J. Appl. Phys. 48 (1977) 3070.
[12] J.G. McGarty, H. Wise, Catal. Today 8 (1990) 231.
[13] Y. Matsuura, S. Matsushima, M. Sakamoto, Y. Sadaoka, J. Mater. Chem. 3 (1993) 767.
[14] E. Traversa, S. Villanti, G. Gusmano, H. Aono, Y. Sadaoka, J. Am. Ceram. Soc. 82 (1999) 2442.
[15] T.M. Rearick, G.L. Catchen, M. Adams, Phys. Rev. B 48 (1993) 224.
[16] D.G. Georgiev, K.A. Krezhov, V.V. Nietz, Solid State Commun. 96 (1995) 535.
[17] G. Martinelli, M.C. Carotta, M. Ferroni, Y. Sadaoka, E. Traversa, Sens. Actuat. B 55 (1999) 99.
[18] A. Sztaniszlav, E. Sterk, L. Fetter, M. Farkas-Jahnke, J. Magn. Magn. Mater. 41 (1984) 75.
[19] S. Nakayama, J. Mater. Sci. 36 (2001) 5643.
[20] N. Pandya, P.G. Kulkanrni, P.H. Parsania, Mater. Res. Bull. 25 (1990) 1073.
[21] D.S. Todorovsky, R.V. Todorovska, St. Groudeva-Zotova, Mater. Lett. 55 (2002) 41.
[22] M. Inoue, T. Nishikawa, T. Nakamura, T. Inui, J. Am. Ceram. Soc. 80 (1997) 2157.
[23] M. Sivakumar, A. Gedanken, W. Zhong, Y.H. Jiang, Y.W. Du, I. Brukental, D. Bhattacharya, Y. Yeshurun, I. Nowik, J. Mater. Chem. 14 (2004) 764.
[24] Q. Ming, M.D. Nersesyan, A. Wagner, J. Ritchie, J.T. Richardon, D. Luss, A.J. Jacobson, Y.L. Yang, Solid State Ionics 122 (1999) 113.
[25] S. Ramanathan, M.B. Kakade, S.K. Roy, K.K. Kutty, Ceram. Int. 29 (2003) 477.
[26] S.M. Zanetti, E.I. Santiago, L.O.S. Bulhoes, J.A. Varela, E.R. Leite, E. Longo, Mater. Lett. 57 (2003) 2812.
[27] Y. Tao, G. Zhao, W. Zhang, S. Xia, Mater. Res. Bull. 32 (1997) 501.
[28] K. Nagashio, K. Kuribayashi, J. Am. Ceram. Soc. 85 (2002) 2550.
[29] O. Yamaguchi, H. Takemura, M. Yamashita, J. Electrochem. Soc. 138 (1991) 1492.
[30] J. Takahashi, E. Matsubara, T. Arima, E. Hanamura, Phys. Rev. B 68 (2003) 155102.
[31] J. Kreisel, P. Bouvier, J. Raman Spectrosc. 34 (2003) 524.
[32] M.N. Iliev, M.V. Abrashev, H.G. Lee, V.N. Popov, Y.Y. Sun, C. Thomsen, R.L. Meng, C.W. Chu, Phys. Rev. B 57 (1998) 2872.
[33] R. Jose, J. James, A.M. John, D. Sundararaman, R. Divakar, J. Koshy, Nanostruct. Mater. 11 (1999) 623.
[34] J.F. Moulder, W.F. Stickle, P.E. Sobol, K.D. Bomben, Handbook of X-ray Photoelectron Spectroscopy, Perkin Elmer Corp, Eden Prairie, MN, 1992.
[35] H. Aono, M. Sato, E. Traversa, M. Sakamoto, Y. Sadaoka, J. Am. Ceram. Soc. 84 (2001) 341.

[36] S. Mathur, M. Veith, R. Rapalaviciute, H. Shen, G.F. Goya, W.L.M. Filho, T.S. Berquo, Chem. Mater. 16 (2004) 1906.
[37] D.S. Schmool, N. Keller, M. Guyot, R. Krishnan, M. Tessier, J. Appl. Phys. 86 (1999) 5712.
[38] P.J. Gellings, H.J.M. Bouwmeester, Catal. Today 58 (2000) 1.
[39] M.S. Palmer, M. Neurock, M.M. Olken, J. Amer. Chem. Soc. 124 (2002) 8452.
[40] W. Zhang, X.X. Wang, X.Z. Fu, Chem. Commun. (2003) 2196.
[41] J. He, W.H. Ma, J.J. He, J.C. Zhao, J.C. Yu, Appl. Catal. B 39 (2002) 211.
[42] C.C. Wong, W. Chu, Environ. Sci. Technol. 37 (2003) 2310.
[43] K.L. Antcliff, D.M. Murphy, E. Griffiths, E. Giamello, Phys. Chem. Chem. Phys. 5 (2003) 4306.